RSC Advances

PAPER

View Article Online
View Journal | View Issue

Cite this: *RSC Adv.*, 2023, **13**, 15041

A comparative study of confinement and layer modified Zr-based MOFs for the efficient removal of Cr(VI) from wastewater

Na Gao,[ab] Qingqing Guan [b] and Zhaoni Kong [*c]

The GO- and SBA-15-modified UiO-66 adsorbents were developed for removal of trace Cr(VI) from wastewater and investigated to understand the effect of different hybrid ways on the absorption activity and reaction mechanism. The characterization results confirmed that the UiO-66 nanoparticles could be encapsulated by the SBA-15 matrix and anchored onto GO layers. Due to different exposure modes, the adsorption results showed that the GO-modified UiO-66 had better Cr(VI) trapping performance with the maximum removal efficiency of 97% within 3 min, presenting one of the most efficient Cr(VI) removal materials. Kinetic models showed that the adsorption process included fast, exothermic, spontaneous and pseudo-secondary chemical adsorption. By comparison with the Freundlich and Temkin model, the results revealed that the adsorption process of Cr(VI) by UiO-66@SBA-15 involved some multi-layer physical adsorption, while Cr(VI) was adsorbed onto the UiO-66@GO surface. The mechanism study also found that the fixation of Cr was the chemical action of UiO-66 on GO. Additionally, the encapsulated way increases the protection of UiO-55 from surface damage. In all, both hard-core–shell UiO-66@SBA-15 and piece UiO-66@Go increase the absorption activity of Cr(VI), but the different hybrid ways lead to different activities, absorption processes and regeneration abilities.

Received 27th February 2023
Accepted 25th April 2023

DOI: 10.1039/d3ra01308a

rsc.li/rsc-advances

1. Introduction

The high harm and toxic effects of heavy metal ions in water bodies have drawn a lot of attention.[1] Cr is one of the widely used heavy metals and can be found in battery production, electroplating, oil refining, alloys, and also industrial wastewater.[2] Cr(III) and Cr(VI) are the two main ion forms of Cr, in which Cr(VI) is a kind of strong carcinogenic and induced ion and can cause a variety of toxic effects. Cr(VI) is limited to 100 ppb drinking water and 200 ppb industrial wastewater by the World Health Organization.[3] Thus, excessive Cr(VI) must be removed from the water. In recent years, various methods to purify Cr(VI) pollution have been used, including ion exchange method,[4] reverse osmosis method,[5] electrodialysis method,[6] chemical precipitation method,[7] membrane separation method,[8] coagulation precipitation method, electrocoagulation precipitation method,[9] and adsorption method.[10] Among them, the adsorption method is a convenient, efficient, and energy-saving treatment method due to its simple process and equipment.

Using porous materials for the adsorption of Cr(VI) is the most promising purification method. Metal–organic frameworks (MOFs) are a new kind of nanoporous crystal material, which have attracted wide attention due to their porous structure, large specific surface area, and active adsorption sites.[11] Several MOFs with different frames have been successfully designed as adsorbents to remove various pollutants from water. For example, zeolite imidazole frame-8 (ZIF-8), which is composed of a Zn(II) cation and 2-methylimidazole anion, has demonstrated good performance in the removal of 1*H*-benzotriazole and 5-tolutriazole.[12] Mil-101, MOFs with terephthalate as organic linker, presents adsorption properties for the removal of organic dyes and separation of olefin paraffin mixtures from aqueous solution. However, there are only a few studies about the adsorption of heavy metals by MOFs. Due to the low chemical potential of Cr(VI) wastewater and the uncertainty of the MOFs surface, the efficiency is low and the adsorption mechanism is unclear. Therefore, more attention has recently been devoted to developing new composites, which can offer a potential capacity to improve the efficiency. For example, MOFs are coordinated with metal nanoparticles, oxide, quantum dots (QDs), metal salts (POMs), polymer, graphene oxide (GO), carbon nanotubes (CNTs), biological molecules, and also mesoporous silica,[13] which can produce new functional composite materials. Compared with a single component, these MOF composite materials have unique properties, showing not only better adsorption properties of

[a]*Faculty of Environmental Science and Engineering, Kunming University of Science and Technology, Kunming, China*
[b]*School of Chemical Engineering and Technology, Xinjiang University, Urumqi, Xinjiang 830046, China*
[c]*School of International Education, Kunming University, Kunming, China. E-mail: 237071828@qq.com*

MOFs but also lower atomic density in the skeleton structure. Additionally, different hybrid methods can make different MOF structures or exposure modes, leading to different surface properties, activities, and reaction mechanisms.

Mesoporous silica is a kind of porous silicon material that can be used to prepare a hard-core–shell MOF material. The combination of mesoporous silica material and microporous crystal MOFs has a broad application prospect in enhancing the mechanical properties and chemical stability. Fang *et al.* have prepared the composite material of hard-core–shell MOF-mesoporous silica.[14] The results indicated that its mechanical stability was better than that of the parent material MOF. However, MOF composite materials containing mesoporous silica have not been fully studied, especially in the confinement effect.[15] Additionally, there is still a lack of knowledge about the adsorption mechanism of heavy metals by the MOF material.

Additionally, GO is a two-dimensional carbon material with rich functional groups, which can be used as a piece filler material for the water purification membrane. The epoxy and hydroxyl functional groups on the edges not only enable them to stably disperse in the solvent for a longer time, but also provide the possibility of forming hydrogen bonds with organic compounds or electrostatic interactions with metal ions.[16] For instance, Yu *et al.* prepared GO/PES. The water flux and anti-fouling performance of the composite membrane were improved due to the hydrophilicity of GO.[17] In addition, GO has significant mechanical properties, which can enhance the mechanical strength of the membrane. Nevertheless, there are still some problems, such as the GO nanosheets piling up easily due to the strong interactions between the adjacent nanoplates. In this regard, it is still challenging to achieve a piece structure to improve the absorption ability, especially for Cr(VI) removal.

In this work, hard-core–shell UiO-66@SBA-15 and piece UiO-66@GO composite materials were developed successfully and the adsorption of Cr(VI) was studied. The work tries to reveal the interaction between different carriers and UiO-66 for the adsorption of Cr(VI), and to give a better understanding of the absorption process by different modified methods: confinement and layer construction. Different adsorption mechanisms of Cr(VI) by the UiO-66@GO and UiO-66@SBA-15 composite materials were proposed through the characterization of the adsorbents. We also built a kinetic model to analyze the effect of different hybrid methods and gain more insight. In all, these data not only provide a new idea for the adsorption of Cr(VI) by composite MOFs, but also reveal the effect of the hybrid method on the structure and activity.

2. Experimental section

2.1. Materials

Zirconium chloride ($ZrCl_4$, AR) and terephthalic acid (H_2BDC, 98%) were used as the zirconium and ligand precursor, respectively. Graphite powder, P_{123}, potassium permanganate ($KMnO_4$, AR), TEOS, nitric acid (HNO_3, AR), sulfuric acid (H_2SO_4, AR), hydrochloric acid (HCl, AR), acetic acid (AA,AR), toluene (AR), potassium dichromate ($K_2Cr_2O_7$, AR), *N*,*N*-dimethylformamide (DMF, AR) and anhydrous ethanol (AR) were purchased from Shanghai Maclean Biochemical Technology CO., LTD. Ultra-pure water was produced using a PSDK System. None of the reagents were further purified.

2.2. Synthesis of UiO-66 nanoparticles

UiO-66 nanoparticles were synthesized by using the method described in the previous literature.[18] A certain amount of $ZrCl_4$ and H_2BDC was added to the mixture of DMF, AA and HCl, then stirred until the solution was opalescent. The solution was poured into the polytetrafluoroethylene reactor liner, reacted at 120 °C for 3 h, washed and filtered with DMF and ethanol, and then dried in vacuum at 80 °C for 24 h.

2.3. Synthesis of GO and SBA-15

GO was synthesized by the modified Hummers' method.[19] A mass of 3.0 g graphite powder and 1.5 g $NaNO_3$ were added to 70 mL concentrated H_2SO_4 and mixed *via* stirring at room temperature, then 9.0 g $KMnO_4$ was gradually added at 273 K. The reaction mixture was stirred at 308 K for 2 h until it became a paste brown. A volume of 140 mL of deionized water was slowly added into the above solution in a water bath, and a further 420 mL of deionized water was added until the temperature dropped. Then, 10 mL 30 wt% H_2O_2 was slowly added into the above solution to neutralize the remaining $KMnO_4$ and the mixture turned a bright yellow color. The mixture was washed and centrifuged with 10% hydrochloric acid solution and deionized water until the pH was about 7, and dried in an oven at 60 °C. For further purification, 2 g of dried fossil oxygen toner was added into 1 L DMF, stirred by ultrasonic centrifugation, and the supernatant was taken to obtain the GO suspension.

SBA-15 was synthesized by a well-known method.[20] P_{123} was added into the mixture of 2 mol L^{-1} HCl solution, and stirred for 1 h at room temperature. Then, 6.4 g TEOS was added dropwise and stirred for 24 h at 40 °C to obtain the opalescent solution, which was poured into the polytetrafluoroethylene reactor lining for 24 h at 100 °C, followed by rinsing and filtering with deionized water and drying at room temperature. Finally, it was calcined in a muffle furnace at 550 °C for more than 5 h.

2.4. Fabrication of UiO-66@GO and UiO-66@SBA-15 composites

The optimized ratio of the GO- and SBA-15-modified UiO-66 was chosen by reference to previous literature.[21–23] The prepared graphene suspension (2 g L^{-1}) was added to the UiO-66 precursor solution (6.1 mL), stirred evenly, and poured into the polytetrafluoroethylene reactor lining for reaction at 120 °C for 3 h, followed by washing and filtration with DMF and ethanol, and vacuum drying at 80 °C for 24 h. The synthesis process of the other composites is that the carrier suspension was prepared with the addition of 1 g SBA-15 into the toluene solution. The precursor solution of UiO-66 was then gradually added. The mixture was stirred evenly, poured into the polytetrafluoroethylene reactor liner, reacted at 120 °C for 3 h, then rinsed and filtered with DMF and ethanol, followed by vacuum

drying for 24 h at 80 °C. Fig. 1 shows the schematic diagram of the synthesis mechanism of the two kinds of composite materials.

2.5. Characterization methods

The Brunauer–Emmett–Teller (BET) specific surface area and pore size were measured by using an automatic surface analyzer. The surface morphologies of the adsorption materials were observed by the field emission scanning electron microscope (SEM) and transmission electron microscopy (TEM). The X-ray diffraction (XRD) patterns were recorded. Fourier transform infrared spectrum (FT-IR) measurements were carried out in a KBr pellet at room temperature. The surface elemental composition analyses were conducted based on the XPS spectra.

2.6. Batch adsorption studies

All adsorption experiments were conducted in a 150 mL beaker under natural pH and light, with the Cr(VI) concentration fixed between 10 mg L^{-1} and 30 mg L^{-1}. Cr(VI) solutions were prepared by dissolving different amounts of $K_2Cr_2O_7$ in deionized water. In all experiments, 50 mL Cr(VI) solution (10 mg L^{-1}) was mixed with 0.05 g adsorbent and stirred at 25 °C with 100 rpm. After a certain amount of time, the mixture was filtered and the filtrate was collected. The absorbance of the Cr solution was detected by spectrophotometer at 540 nm using the national standard method, *i.e.*, 1,5-diphenyl carbonyl dihydrazide measurement method. The concentration of the Cr solution was obtained by comparing the relationship between the absorbance and concentration. The adsorbent was collected and dried overnight in vacuum at 80 °C for characterization.

The properties of the adsorbed materials were evaluated by removal rate and adsorption capacity. The removal rate of Cr(VI) was calculated according to the formula:

$$\text{percent of} = \frac{C_0 - C_t}{C_0} \times 100\% \quad (1)$$

The adsorption amount of Cr(VI) on the adsorbent was calculated according to the formula:

$$Q_t = \frac{(C_0 - C_t) \times V}{m} \quad (2)$$

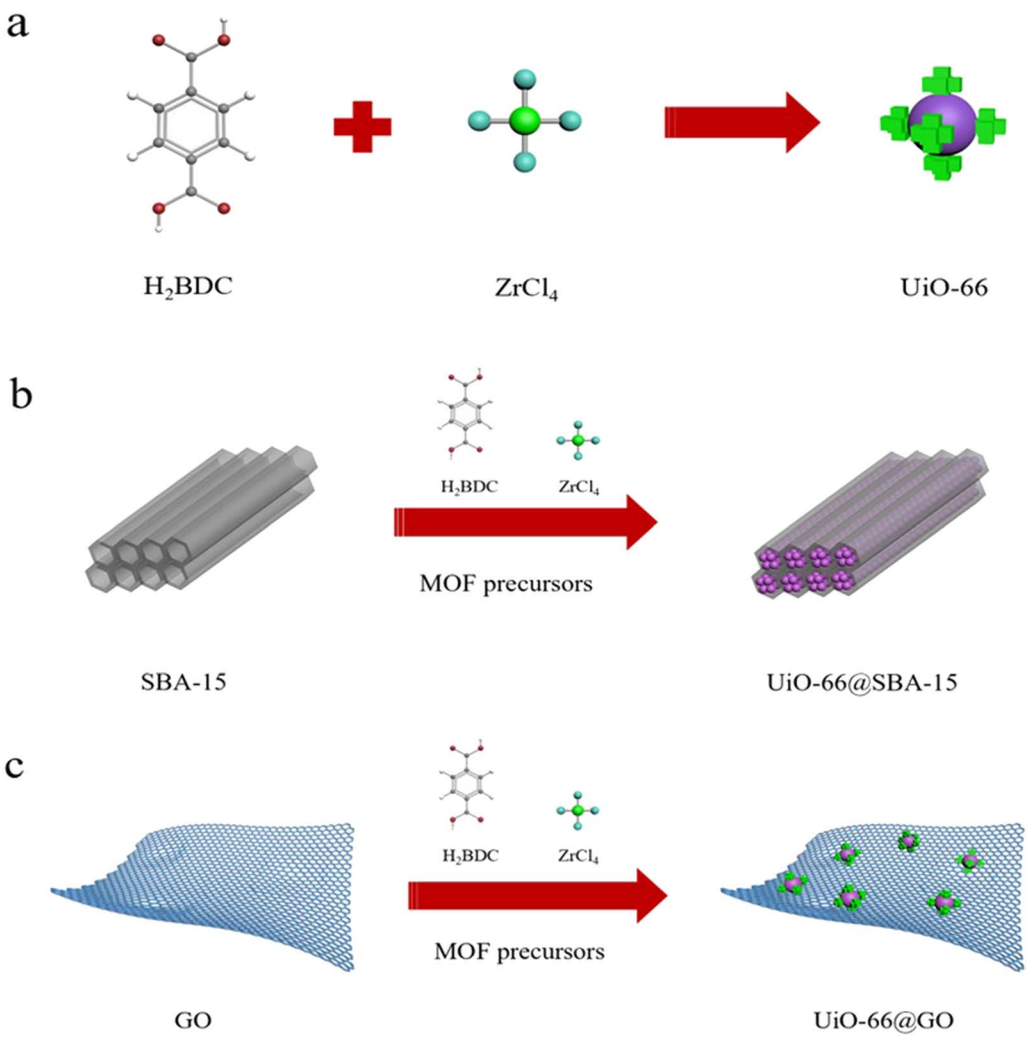

Fig. 1 Proposed synthesis route of (a) UiO-66, (b) UiO-66@SBA-15 and (c) UiO-66@GO composites.

where, C_0 and C_t are the concentration of the initial Cr(VI) (mg L^{-1}) and the concentration of Cr(VI) at the time of contact with t, respectively. V is the solution volume (mL), and m is the mass (g) of the adsorbent added. All experiments were repeated.

3. Results and discussion

3.1. Characterizations

3.1.1. Characterization of the UiO-66@SBA-15 composite. To study the morphologies, SEM and TEM analyses of the compounds were carried out. Fig. 2a shows that the composite material does not differ much from the size of SBA-15, indirectly indicating that the UiO-66 nanoparticles are likely to be encapsulated in the pores of SBA-15. To prove that, TEM images of composites were recorded. Fig. 2b shows the pore structure, and Fig. 2c is the point scan image of the composite material shown in Fig. 2b. From the analysis of the peak position, Si and Zr elements can be found, which comes from the SBA-15 and UiO-66. It is clear that most of the UiO-66 exist in the mesopores of SBA-15, indicating that the nucleation of UiO-66 is well wrapped in the channel of SBA-15, although they are not exactly evenly distributed and in good crystallization forms. A plausible mechanism of the growth of the UiO-66 nanocrystals in the hole of SBA-15 has been presented in Fig. 1b. The precursors of UiO-66 have been firstly added to the SBA-15 matrix, and the nucleation of UiO-66 in the pore is more favorable than that outside the SBA-15 due to the inner surface affinity of the silanol groups.[24] The periodically arranged large pores also promote the rapid diffusion of the UiO-66 precursor solution into the pores and the formation of composite materials.

Fig. 2d shows the XRD patterns of UiO-66 and the UiO-66@SBA-15 composite, which also confirmed that UiO-66 was successfully synthesized in the channel of SBA-15. The morphology of UiO-66 is consistent with that reported in the literature, which indicates that the synthesis of UiO-66 was successful.[18] UiO-66@SBA-15 has the same characteristic peaks as UiO-66 on the SBA-15 hill-type peaks, indicating that the crystal structure of UiO-66 in the composite material is not changed during crystallization.[25]

The N_2-adsorption–desorption curves of SBA-15 and UiO-66@SBA-15 are shown in Fig. 2e and f. Both samples have IV adsorption isotherms and H1 hysteresis loops, indicating good mesoporous junctions. The pore distribution of the two samples is 6.8 nm for SBA-15 and 5.7 nm for UiO-66@SBA-15. The decrease of the pore diameter of the composite indicates that the nanocrystalline material has filled the mesopore of the composite.

3.1.2. Characterization of the UiO-66@GO composite. The N_2-adsorption–desorption curves of UiO-66 and UiO-66@ GO are shown in Fig. 3a and b. Both samples have I adsorption isotherms, indicating microporous junctions. The decrease of the pore diameter was also observed, indicating the presence of GO with UiO-66. The morphology of the UiO-66@GO composite was also investigated by SEM and TEM, as shown in Fig. 3c and d. The UiO-66 nanoparticles and GO layer can been observed, showing the presence both GO and MOF complex, which is distributed in an orderly manner on the GO layer. Petit and Bandosz reported on the MOF–GO composites and have compared them with the physically mixed samples.[26] The order distribution indicates that the UiO-66 nanoparticles have been fixed on the GO layer by epoxy groups, while physically mixing with GO usually leads to agglomerates and an uneven distribution. The addition of UiO-66 has also avoided the layer stacking of GO. For further confirmation, energy dispersive X-ray spectroscopy (EDX) analysis (Fig. 3e and f) of the composites was conducted. The results show the presence of C, O and Zr elements. Furthermore, the elemental mapping (Fig. 3f) suggests that different elements in the sample are evenly distributed, proving the successful synthesis of the UiO-66@GO composite.

Fig. 3g shows the XRD patterns of UiO-66 and the UiO-66@GO composite. The pattern of UiO-66 is in good agreement with that reported in the literature, indicating the successful synthesis.[27] The identical peaks of UiO-66@GO with UiO-66 demonstrate that the crystalline structure of UiO-66 in the composite material has not been changed during the *in situ* crystallization. It should be noted that the GO peak at 2θ is about 9.29°, which shows some overlap with the UiO-66 peak.[26] A very slight change of sharpness at about 9.78° can been observed, which is in agreement with Li's results.[22]

3.2. Adsorption activity

Removal of Cr(VI) from wastewater by UiO-66@SBA-15 and UiO-66@GO was compared under different conditions, *i.e.*, different pH, temperature and initial concentration factors. Fig. 4 shows the relationship between the equilibrium adsorption capacity (q_e) and equilibrium Cr(VI) concentration (C_e) in solution at different temperatures. UiO-66@GO has higher Cr(VI) removal activity than UiO-66@SBA-15, presenting one of the most efficient Cr(VI) removal materials. The equilibrium Cr(VI) adsorption capacity by SBA-15 and UiO-66 was 5.3 mg g^{-1} and 15 mg g^{-1}, respectively. Thus, both UiO-66@GO and UiO-66@SBA-15 have higher Cr(VI) removal efficiency than the single SBA-15 and UiO-66, indicating that the functionalized carrier structural modification can improve the MOFs removal activity of Cr(VI). Additionally, the adsorption capacity of UiO-66@SBA-15 decreased from 13.77 mg g^{-1} to 11.27 mg g^{-1}, and the adsorption capacity of UiO-66@GO decreased from 38.13 mg g^{-1} to 32.91 mg g^{-1} as the temperature increased, which indicates that high temperature is not conducive to the adsorption of the two composites. Although the higher initial Cr(VI) concentration leads to higher adsorption capacity of equilibrium, it is also clear that the removal rate of UiO-66@SBA-15 and UiO-66@GO decreased from 61% to 38% and 97% to 80% with an initial concentration of Cr(VI) increasing from 10 to 30 mg L^{-1}, respectively, as shown in Fig. 5. The maximum removal efficiencies of UiO-66@SBA-15 and UiO-66@GO were 61% and 97%, respectively, when the concentration of Cr(VI) was 10 mg L^{-1}. In all, the piece structure UiO-66@GO has higher activity than the hard-core–shell UiO-66@SBA-15 due to there being more active site exposure.

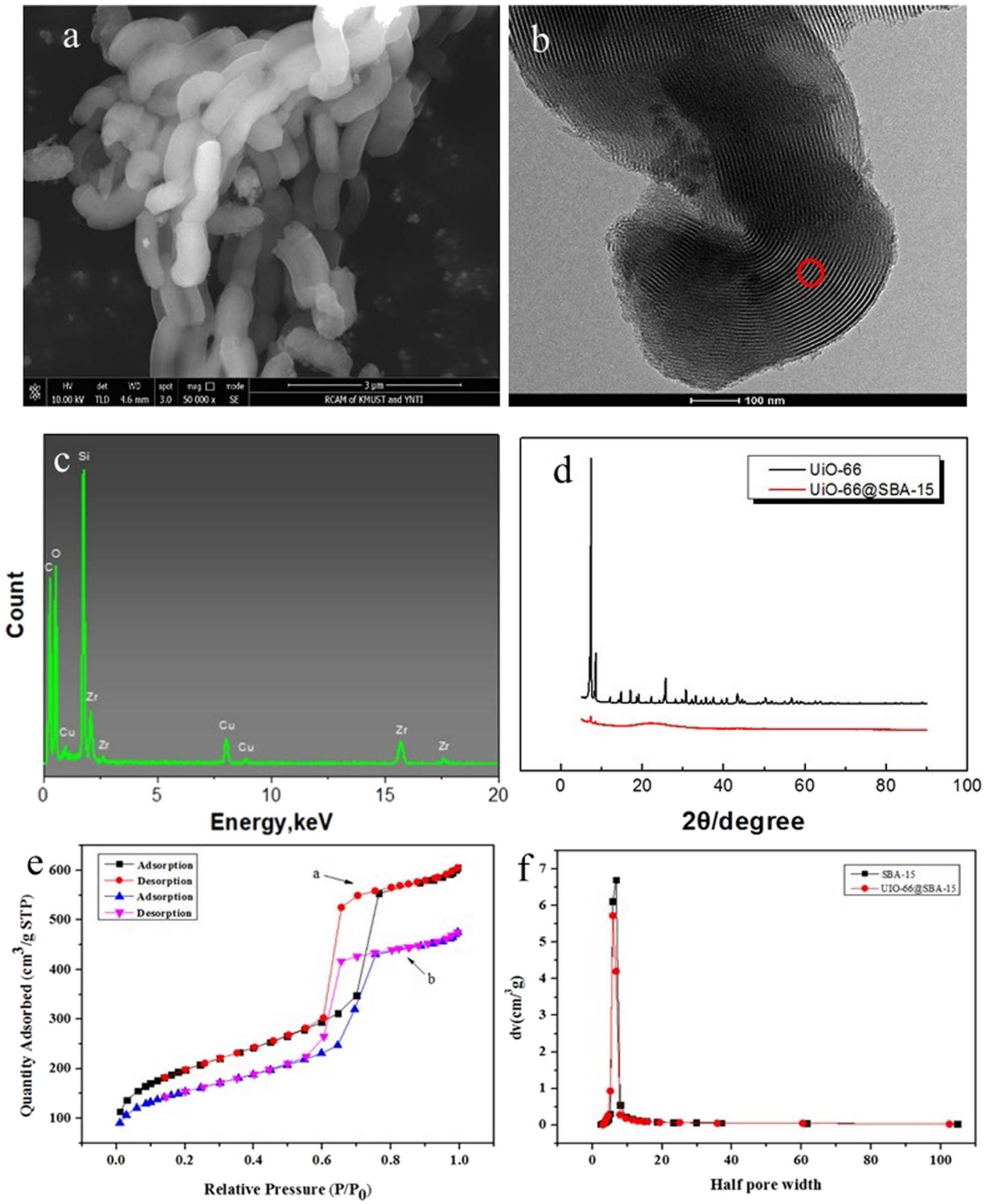

Fig. 2 (a)–(c) SEM and TEM (EDS) images of UiO-66@SBA-15, (d) PXRD patterns of UiO-66 and UiO-66@SBA-15, and (e) and (f) N_2 adsorption isotherms and pore size distribution of SBA-15 and UiO-66@SBA-15.

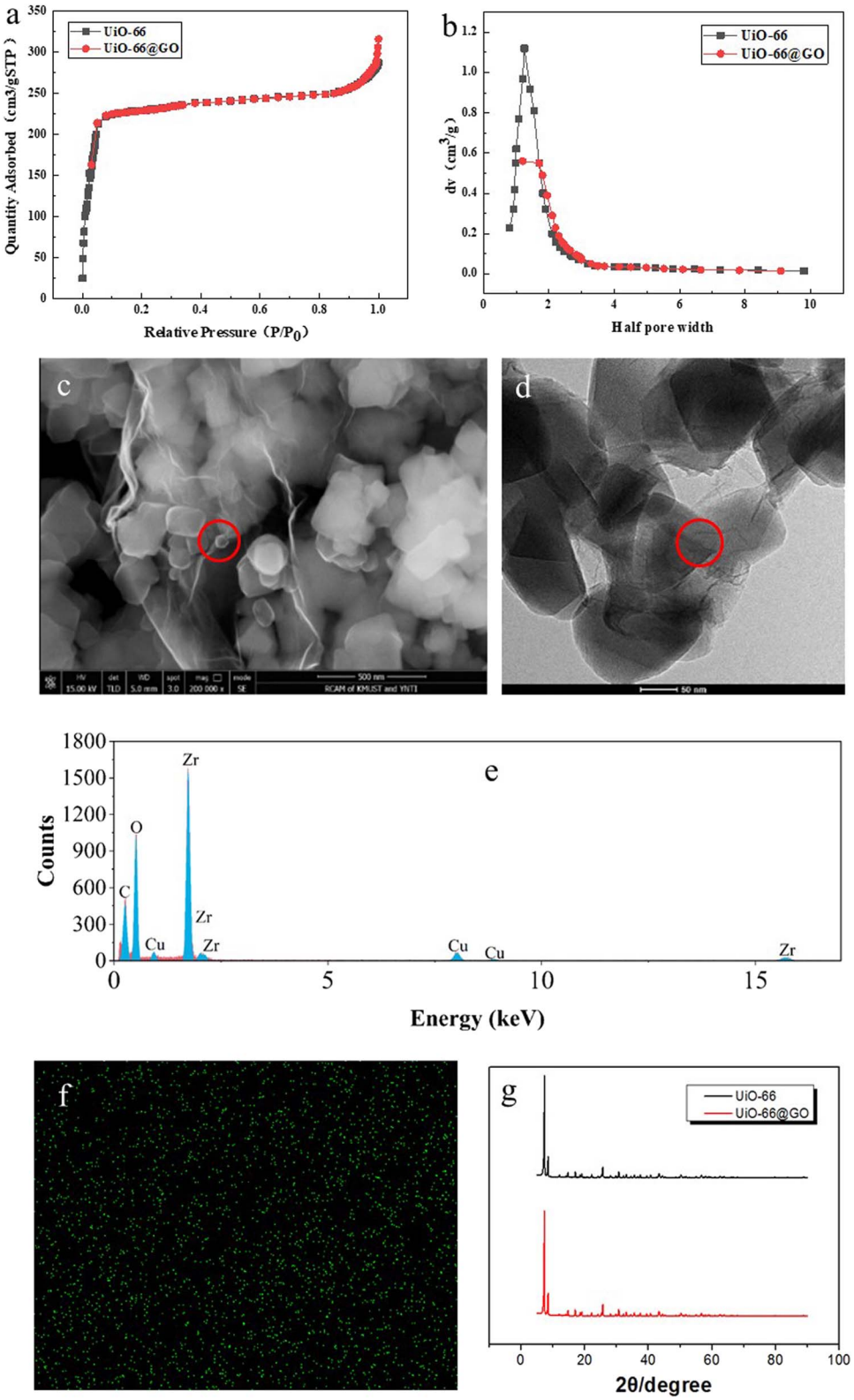

Fig. 3 (a) N_2 adsorption isotherms and (b) pore size distribution, (c) SEM and (d) TEM images of the UiO-66@GO, (e) EDS of the UiO-66@GO, (f) EDX mapping images of UiO-66@GO, and (g) PXRD patterns of UiO-66 and UiO-66@GO.

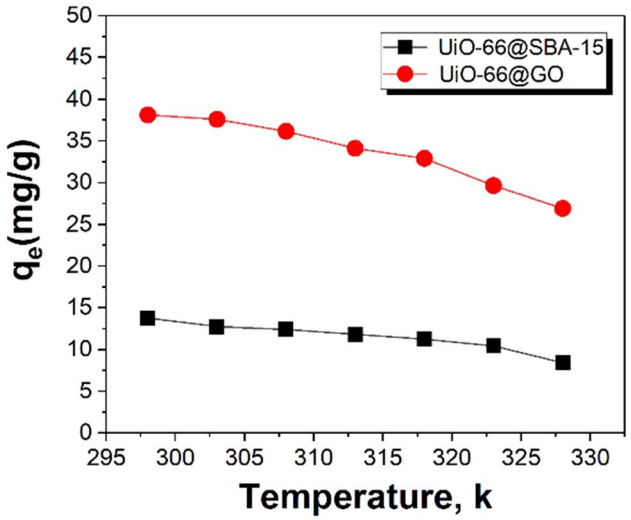

Fig. 4 Effect of temperature on the adsorption of Cr to UiO-66@SBA-15 and UiO-66@GO.

3.3. Kinetic model

In order to better analyze the effects of the two composite materials on the Cr(VI) adsorption properties, three kinetic models were selected for simulation. The initial concentration of Cr(VI) was fixed at 10–30 mg L^{-1}, and UiO-66 was loaded with 10 wt% GO and SBA-15 was loaded with 10 wt% UiO-66. The adsorption kinetics was tested by using the linear diagram of pseudo-first-order, pseudo-second-order and intra-particle diffusion kinetic models.

The pseudo-first-order model is used in the adsorption process, and its expression is as follows:[28]

$$\log(q_e - q_t) = \log q_e - \frac{k_1}{2.303t}$$

where q_e and q_t are the adsorption capacity of the composite for Cr(VI) at equilibrium and instant time t (h), respectively. k_1 is the rate constant of the pseudo-first-order adsorption (h^{-1}). k_1 and q_e is calculated from the slope and intercept of the plots of $\log(q_e - q_t)$ *versus* t, respectively. The related parameters are presented in Table 1. There is a significant difference between the calculated q_e and the experimental q_e. The low correlation coefficient R^2 (Tables 1 and 2) has been found, showing that the adsorption of Cr(VI) into the composite fit poorly with the pseudo first-order kinetic model.

Table 1 Adsorption kinetics parameters of Cr(VI) onto UiO-66@SBA-15

	Parameters		
Kinetic models	Q_{eq}	k	R^2
Pseudo-first-order kinetic model	6.18582	1.59742	0.81824
Pseudo-second-order kinetic model	6.27549	0.09826	0.99989
Intra-particle-diffusion models	7.87176	0.43451	0.75662

The pseudo-second-order equation can be expressed by the following equation:[29]

$$\frac{t}{q_t} = \frac{1}{k_2 q_e^2} + \frac{t}{q_e} \quad (3)$$

where k_2 (g mg^{-1} h^{-1}) is the rate constant of the pseudo-second-order adsorption determined by plotting t/q_t *versus* t. The plots of t/q_t against t at different initial Cr(VI) concentrations are shown in Fig. 6b and 7b, and the values of the parameters are summarized in Tables 1 and 2. The data show an excellent fit to the pseudo-second-order model with high R^2 (>0.999). A good fit was also further confirmed by the fact that the calculated q_e value is very close to the measured one.

Since the above kinetic model cannot determine the diffusion mechanism or the rate control process that might affect the kinetics of adsorption, the intra-particle diffusion was further studied. The intra-particle diffusion model is the empirical function relationship of the adsorption amount at interval t (q_t) and $t^{1/2}$. The velocity parameter relationship of the intra-particle diffusion can be determined by the following equation:[30]

$$q_t = k_{id} t^{1/2} + C_i \quad (4)$$

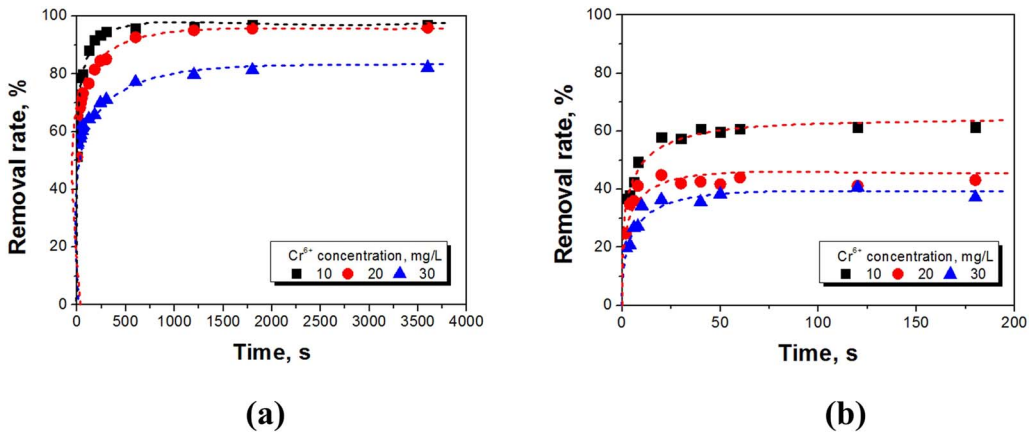

Fig. 5 Effect of the initial Cr(VI) concentration on the adsorption of Cr(VI) to (a) UiO-66@SBA-15 and (b) UiO-66@GO.

Table 2 Adsorption kinetics parameters of Cr(VI) onto UiO-66@GO

	Parameters		
Kinetic models	Q_{eq}	k	R^2
Pseudo-first-order kinetic model	8.38012	1.64234	0.73983
Pseudo-second-order kinetic model	7.51314	0.02072	0.99994
Intra-particle-diffusion models	6.49401	0.10612	0.93364

where k_{id} is the intra-particle diffusion rate constant (mg g^{-1} h$^{-1/2}$), and C_i is the intercept related to the thickness of the boundary layer. In general, the larger the intercept, the greater contribution of the surface adsorption to the rate control.

The dynamic curves and parameters of the three models of the two materials are shown in Fig. 6, 7, Tables 1 and 2. The pseudo-second-order correlation coefficients ($R^2 > 0.999$) of UiO-66@SBA-15 and UiO-66@GO are both higher than that of the pseudo-first-order (R^2) and intraparticle diffusion dynamics model (R^2), indicating that the experimental data of both groups are applicable to pseudo-second-order models. The data are in good agreement with the model, indicating that the adsorption of Cr(VI) by the two materials is closer to chemical adsorption; that is, the total adsorption rate is controlled by the electron sharing or exchange between the adsorbent and adsorbate.[31] Thus, piece or encapsulated structure modification has not changed the adsorption type.

Additionally, the presence of functionalized carriers and active sites of UiO-66 have increased the adsorption rate. Adsorption is usually achieved by surface diffusion and intra-particle diffusion. However, the correlation coefficient of the intraparticle diffusion model shows that the intraparticle diffusion mechanism does not dominate the rate determination step. Low C_i corresponds to high contribution intraparticle diffusion. If C_i equals zero, the adsorption is completely controlled by intraparticle diffusion. For all of the tested Cr concentrations, the C_i values of the linear parts are not zero, which indicates that intraparticle diffusion is a part of the diffusion process, but it is not the only rate-controlled step in all stages.[32]

3.4. Adsorption isotherms

In order to better analyze the adsorption thermodynamics of Cr(VI) on UiO-66@GO and UiO-66@SBA-15, three adsorption

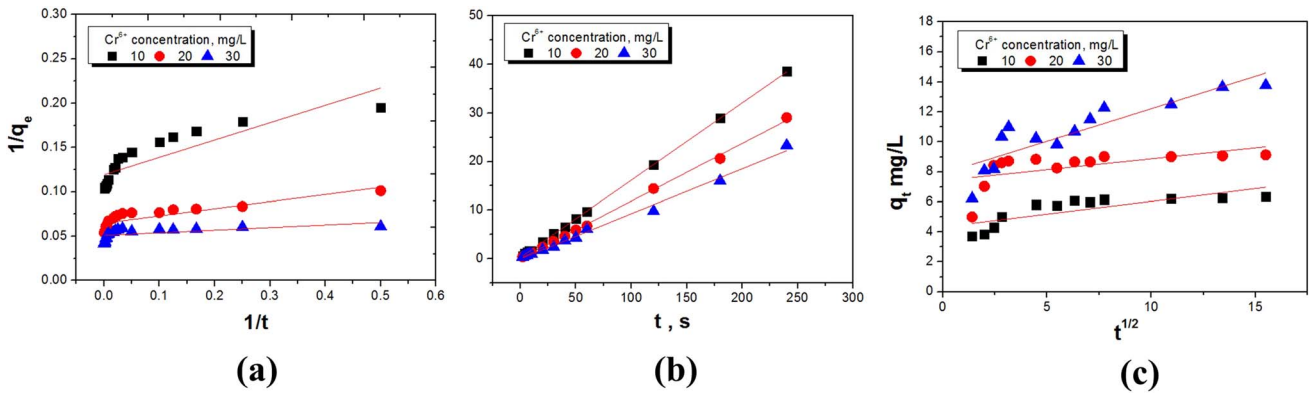

Fig. 6 (a) Pseudo-first-order kinetic fitting, (b) pseudo-second-order kinetic fitting, and (c) intra-particle diffusion kinetic fitting for the adsorption of Cr(VI) onto UiO-66@SBA-15 (solution volume = 50 mL, adsorbent dose = 0.05 g, initial Cr(VI) concentration = 10–30 mg L^{-1}, at natural pH, contact time = 1 h, T = 298 K).

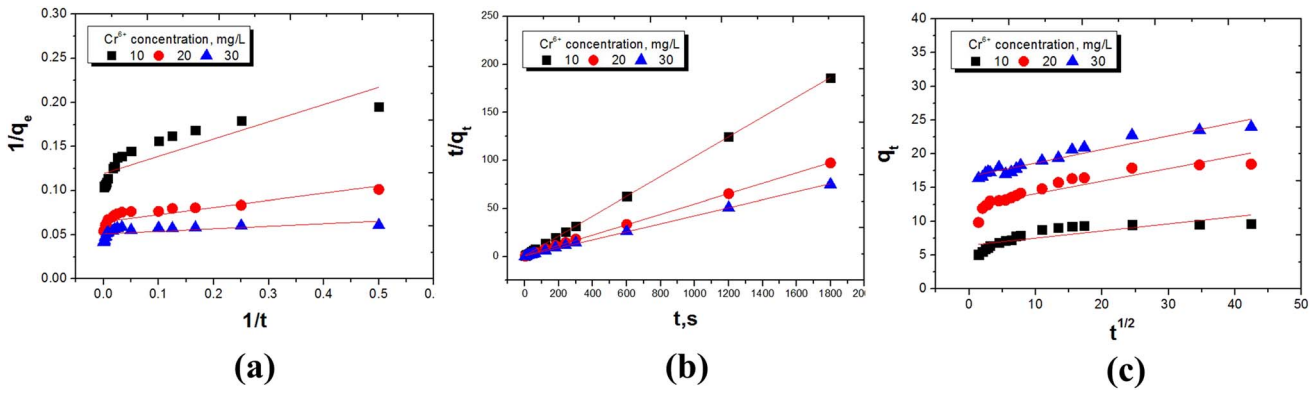

Fig. 7 (a) Pseudo-first-order kinetic fitting, (b) pseudo-second-order kinetic fitting, and (c) intra-particle diffusion kinetic fitting for the adsorption of Cr(VI) onto UiO-66@GO (solution volume = 50 mL, adsorbent dose = 0.05 g, initial Cr(VI) concentration = 10–30 mg L^{-1}, at natural pH, contact time = 1 h, T = 298 K).

isotherm equations of Langmuir, Freundlich and Temkin were adopted according to the adsorption equilibrium data. The express of Langmuir equation is:[33]

$$\frac{C_e}{q_e} = \frac{C_e}{q_{max}} + \frac{1}{q_{max} K_L} \quad (5)$$

where q_e is the amount of Cr(VI) adsorbed at equilibrium (mg g^{-1}), q_{max} is the maximum adsorption amount corresponding to the complete single-layer coverage (mg g^{-1}), C_e is the equilibrium concentration of the solution (mg L^{-1}), and K_L is the Langmuir constant related to the affinity and adsorption energy of the binding site (L mg^{-1}).

C_e/q_e has a linear relationship with C_e (Fig. 8a and 9a), and the Langmuir isotherm constants K_L and q_{max} are shown in Tables 3 and 4. The Langmuir equation can fit the correlation coefficient $R^2 \geq 0.97$ of experimental data. The q_{max} and K_L decrease with an increase in temperature due to the exothermic nature of the adsorption process. Another parameter R_L is given by the following equation:[34]

$$R_L = \frac{1}{1 + K_L C_0} \quad (6)$$

where C_0 is the highest initial concentration of Cr (mg L^{-1}). Different values of R_L represent different meanings: when $R_L >$ 1, the isotherm is unfavorable; it is favorable when $R_L < 1$; when $R_L = 1$, the isotherm is linear; and it is irreversible when $R_L = 0$. In this study, the R_L values obtained by fitting the measured data of UiO-66@SBA and UiO-66@GO ranges between 0.03 and 0.056, indicating that adsorption is a good process. Those results are generally consistent with the chemical monolayer adsorption by both UiO-66@SBA and UiO-66@GO, indicating that exchange between Cr(VI) and UiO-66 is the main contribution to the adsorption process.

The Freundlich isotherm is based on the empirical equation that adsorption occurs on heterogeneous surfaces. The equation is:[35]

$$\ln q_e = \ln K_F + \frac{1}{n} \ln C_e \quad (7)$$

where K_F is a Freundlich constant related to the adsorption capacity (L mg^{-1}), and $1/n$ is the heterogeneity factor to evaluate the adsorption process. A linear relationship between $\ln q_e$ and $\ln C_e$ has been obtained, as shown in Fig. 8b and 9b. The Freundlich parameters K_F and N are calculated based on the regression slope and intercept, as shown in Tables 3 and 4. It is clear that UiO-66@SBA-15 has a high fitting degree with the Freundlich model but that of UiO-66@GO is relatively weak, indicating that the process of Cr(VI) adsorption carried out by

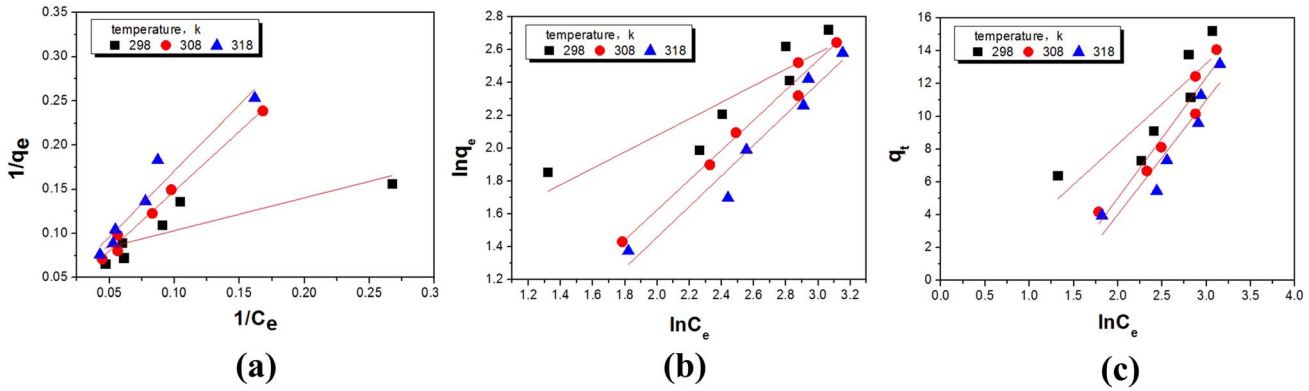

Fig. 8 (a) Langmuir, (b) Freundlich, and (c) Tempkin isotherms for the adsorption of Cr(VI) onto UiO-66@SBA-15 (solution volume = 50 mL, adsorbent dose = 0.05 g, initial Cr(VI) concentration = 10–50 mg L^{-1}, at natural pH, contact time = 1 h, T = 298 K).

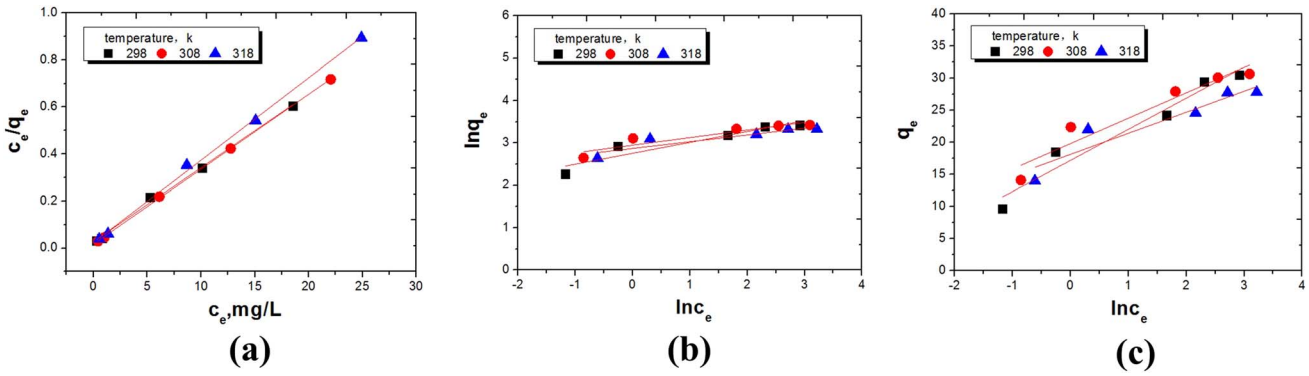

Fig. 9 (a) Langmuir, (b) Freundlich, and (c) Tempkin isotherms for the adsorption of Cr(VI) onto UiO-66@GO (solution volume = 50 mL, adsorbent dose = 0.05 g, initial Cr(VI) concentration = 10–50 mg L^{-1}, at natural pH, contact time = 1 h, T = 298 K).

Table 3 Isotherm parameters for the adsorption of Cr(VI) onto UiO-66@SBA-15

Isotherms	Parameters	
Langmuir	Q_{eq}	358.32
	K_L	0.06
	R^2	0.98
Freundlich	K_F	188.78
	N	6.75
	R^2	0.97
Tempkin	K_T	112.67
	B_T	48.31
	R^2	0.86

Table 4 Isotherm parameters for the adsorption of Cr(VI) onto UiO-66@GO

Isotherms	Parameters	Value
Langmuir	Q_{eq}	30.88
	K_L	0.66
	R^2	0.98
Freundlich	K_F	17.09
	N	4.54
	R^2	0.89
Tempkin	K_T	100
	B_T	4.85
	R^2	0.94

UiO-66@SBA-15 involves not only monomolecular chemical adsorption, but also multi-layer physical adsorption. Thus, the mesopores of SBA-15 increase the physical adsorption of Cr(VI), while GO has little effect on the physical adsorption.

The Temkin isotherm is based on the hypothesis that there exists adsorption–adsorption interaction. The heat of adsorption decreases linearly with coverage due to this interaction. The isotherm is expressed as follows:[36]

$$q_e = B_T \ln K_T + B_T \ln C_e \quad (8)$$

where $B_T = RT/b_T$ and b_T (J mol^{-1}) is the Temkin constant related to the heat of adsorption, R is the gas constant (8.314 J mol^{-1} K^{-1}) and T is the temperature (K), K_T (L mg^{-1}) is the binding energy constant, q_e (mg g^{-1}) and C_e (mg L^{-1}) are the adsorption equilibrium capacity and adsorption equilibrium concentration, respectively. The linear regression curves of q_e *versus* $\ln C_e$ are shown in Fig. 8c and 9c, and the calculated values of B_T, b_T and K_T are shown in Tables 3 and 4. The results show that the fitted Tempkin curve deviates from the linear relationship at all temperatures. According to the relevant diagram of the fitting, the correlation coefficients (R^2) range is 0.86 to 0.94. The lower value of b_T indicates that the interaction of Cr(VI) with UiO-66@SBA-15 and UiO-66@GO is weak. The adsorption process of UiO-66@GO also has a higher fitting degree with the Tempkin model. The adsorption process of UiO-66@GO was better fit by both Langmuir and Tempkin models, confirming that the adsorption of Cr by UiO-66@GO is adsorbed not only as monomolecular chemical adsorption, but also surface adsorption.

3.5. Thermodynamic study

The influence of temperature on the adsorption of Cr(VI) on UiO-66@SBA-15 and UiO-66@GO was further estimated. The thermodynamic parameters, including the Gibbs free energy (ΔG^0), enthalpy (ΔH^0), and entropy (ΔS^0), were determined by the following equations:

$$\Delta G^0 = -RT \ln b \quad (9)$$

$$\Delta H^0 = RT_1 - T_1 \ln\left(\frac{b_2}{b_1}\right) \quad (10)$$

$$\Delta S^0 = \frac{\Delta H^0 - \Delta G^0}{T} \quad (11)$$

where R (8.314 J mol^{-1} K^{-1}) is the gas constant. T (K) is the absolute temperature, and b is the Langmuir constant at T. K is the adsorption equilibrium constant. The calculated values of ΔG^0, ΔH^0, and ΔS^0 at 298, 308 and 318 K with the initial concentration of 10 mg L^{-1} are shown in Table 5.

The free energy values (ΔG^0) are negative, indicating that the reaction of the metal ions promote the spontaneous absorption of Cr(VI). However, with the increase of temperature, ΔG^0 increases, indicating that the increase of temperature does not make it easier for absorption. As S^0 gets larger, it is more favorable for the spontaneous absorption. With the increase of temperature, the value of S^0 decreases, indicating that heating makes the forward absorption more difficult. Thus, the adsorption of Cr(VI) is a spontaneous reaction, but the increase of temperature does not promote the adsorption process. Moreover, the properties of physical adsorption or chemical adsorption can be determined by the free energy value. In general, the value of energy ΔG^0 between 0 and −20 kJ mol^{-1} indicates that the adsorption process is physical adsorption, and the value between −80 and −400 kJ mol^{-1} corresponds to chemical absorption.[37] In this study, the adsorption of UiO-66@SBA-15 and UiO-66@GO by Cr(VI) may include both physical adsorption and chemical adsorption, since ΔG^0 is lower than −20 kJ mol^{-1}, but higher than −80 kJ mol^{-1}. The results are consistent with the adsorption isotherm model.

3.6. Adsorption mechanism

The elemental compositions of the two adsorbents after absorption of Cr were analyzed by XPS to further study the interaction between the adsorbent and Cr(VI). From Fig. 10a and c, it can be

Table 5 Adsorption isotherm parameters for Cr(VI) on UiO-66@SBA-15 and UiO-66@GO

	Temp. (K)	ΔG^0 (kJ mol^{-1})	ΔH^0 (kJ mol^{-1})	ΔS^0 (J mol^{-1} K^{-1})
UiO-66@SBA-15	298	−27.25	27.63	184.16
	308	−25.71		173.18
	318	−23.40		160.47
UiO-66@GO	298	−35.48	27.02	209.71
	308	−34.67		200.29
	318	−32.64		187.61

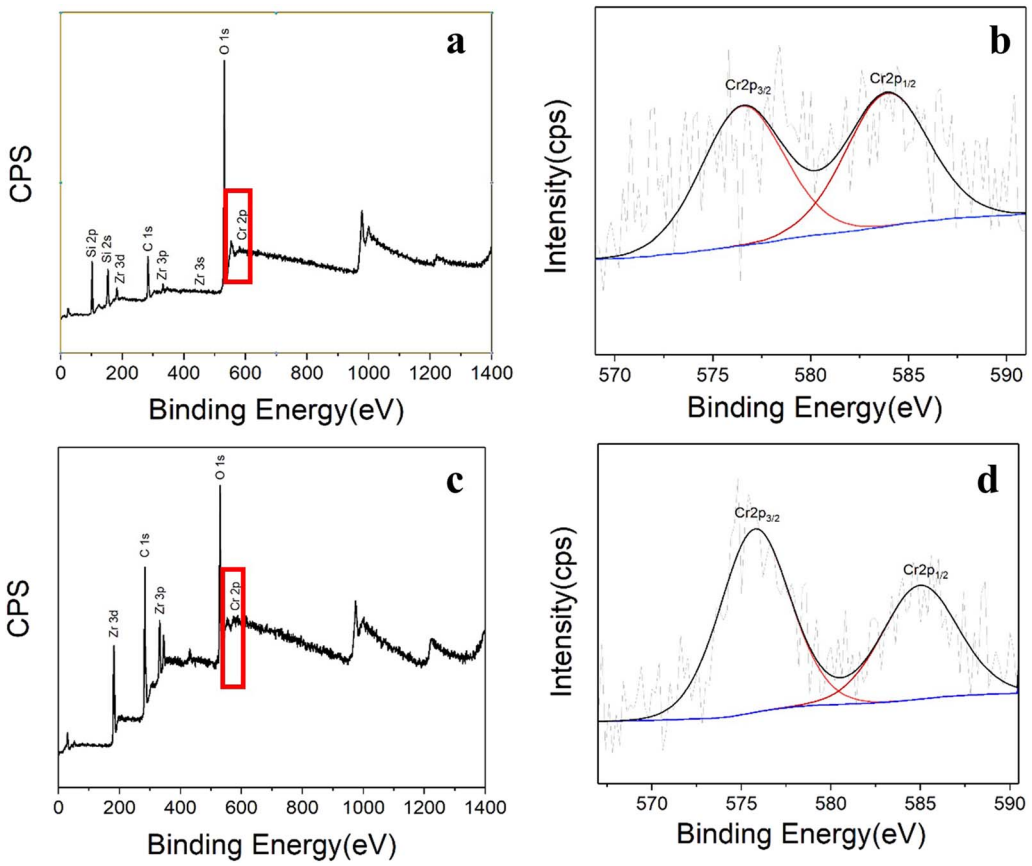

Fig. 10 (a) XPS survey spectra and (b) Cr 2p core level spectra of UiO-66@SBA-15 after adsorption. (c) XPS survey spectra and (d) Cr 2p core level spectra of UiO-66@GO after adsorption.

seen that the two adsorbents contain not only the elements of the adsorbent itself, but also elements Cr, indicating that Cr in the wastewater has been fixed by the adsorbent, which further proves the chemical adsorption of Cr(VI) by UiO-66@SBA-15 and UiO-66@GO. The high resolution Cr 2p XPS spectra of the two adsorbents adsorbed by Cr(VI) are shown in Fig. 10b and d. The two energy peaks of UiO-66@SBA-15 and UiO-66@GO adsorbents are 576.53 eV and 583.89 eV, 575.75 eV and 584.97 eV, respectively, corresponding to Cr $2p_{3/2}$ and Cr $2p_{1/2}$.[19] For UiO-66@SBA-15, it can be seen that Cr mainly exists in CrO_x (576.5 eV) and Cr_2O_3 (576.5 eV) according to the position of the peaks. It is clear that the fixation of Cr has the effect of UiO-66 on SBA-15, showing both chemical adsorption and physical adsorption. For UiO-66@GO, the energy peak is 575.7 eV, which is lower than that of UiO-66 on SBA-15, indicating some electron trajectory deviation and a stronger action between Cr(VI) and UiO-66@GO.[38]

To further understand the mechanism of adsorption, Fourier transform infrared spectroscopy (FTIR) was used. As shown in Fig. 11a, the wide bands of about 3477 cm^{-1} and 1654 cm^{-1} correspond to the stretching vibration of the O–H groups of water.[39] The bands at 1088 cm^{-1} and 467 cm^{-1} belong to the bending vibrations of the mesoporous skeleton (Si–O–Si).[40] In addition, the peak at 910 cm^{-1} is attributed to the Si–OH bond stretching of the silanol groups.[41] The weak band detected at 1680 cm^{-1} is allocated to the stretching vibrations of C≡O in carboxylic acid of BDC.[42] The O–C–O (1588 cm^{-1}), C≡C (1504 cm^{-1}), benzene ring (1416 cm^{-1}) by the BDC ligand have also been found.[43] The main change is the weakening of the peak at 1396 cm^{-1}, confirming the coordination between the carboxylate functional group with metal cations, which indicates the exchange absorption of Cr(VI) by UiO-66@SBA-15.

Fig. 11b shows the FTIR spectra of UiO-66@GO before and after the adsorption. Compared with the spectra before and after Cr(VI) sorption, the Cr=O band arose at 870 cm^{-1}, showing that the oxygen functional groups on the GO layers have bound to the open metal sites of UiO-66, resulting in the disappearance of the GO band.[24] After Cr(VI) absorption, some changes of functional groups on the composite materials can been observed. It should be noted that the results show the Cr(VI) reduction by the carboxylic acid groups on C during absorption, confirming the chemical reaction between Cr(VI) and UiO-66@GO once again.

3.7. Reusability of UiO-66@SBA-15 and UiO-66@GO

Regeneration and reuse capabilities are important for the potential control of the performance of the adsorbent systems. Since high pH has a detrimental impact on the adsorption of Cr(VI), the desorption of Cr(VI) ions might be achieved by the increase of pH. The Cr(VI) desorption experiment was conducted with 0.5 M NaOH. The results of five consecutive adsorption/

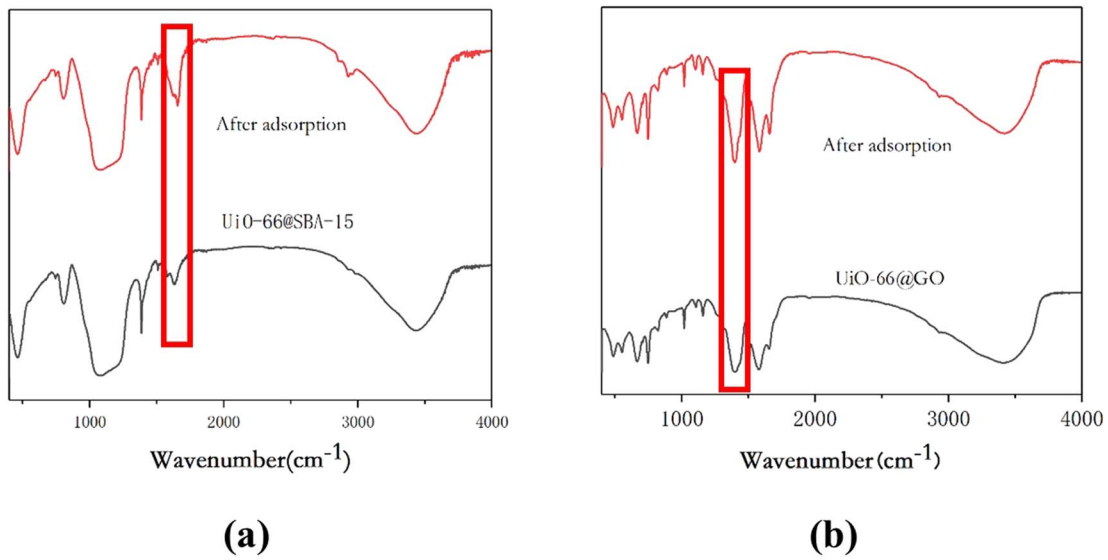

Fig. 11 (a) FITR spectra for (a) UiO-66@SBA-15 and after adsorption, (b) UiO-66@GO and after adsorption.

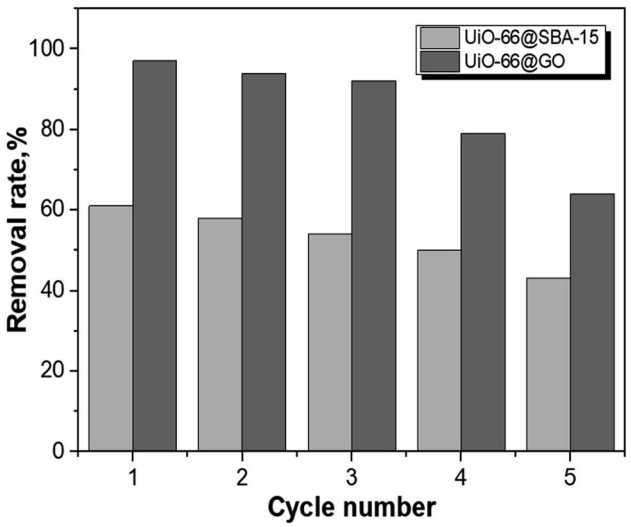

Fig. 12 The reusability of UiO-66@SBA-15 and UiO-66@GO for the adsorption of Cr(VI).

desorption cycles are shown in Fig. 12, and the removal efficiency of both materials was gradually decreased. The reason might be that the adsorption sites on the surfaces could be damaged by multiple adsorption–desorption cycles. However, the removal of UiO-55@SBA-15 has a relatively stable decreasing frequency, indicating that the encapsulated method does protect UiO-55 from surface damage. In addition, for UiO-66@GO, although the removal efficiency was lowered, it remained at a level of 60% after the fifth cycle.

4. Conclusions

Two new adsorbents, UiO-66 immobilized by SBA-15 and GO, were prepared and compared for the removal of low-concentration Cr(VI) from water. The adsorption performance of functionalized UiO-66 was significantly improved. When the initial concentration of hexavalent Cr was fixed at 10 mg L^{-1}, it was observed that only 3 minutes was necessary to reach the equilibrium. For UiO-66@GO, the adsorption efficiency was up to 97%, higher than other equivalent adsorption materials. To understand the mechanism, the pseudo-first-order, pseudo-second-order and intra-particle diffusion kinetic models were fitted. The adsorption of Cr(VI) by both materials was closer to chemical adsorption, and the total adsorption rates were increased and controlled by the electronic sharing or exchange between the adsorbent and the adsorbate. The Langmuir model showed that exchange between Cr(VI) and UiO-66 was the main contribution to the adsorption process. By comparing it with the Freundlich and Temkin models, the results revealed that the adsorption process of Cr(VI) by UiO-66@SBA-15 involved not only monomolecular chemical adsorption, but also multi-layer physical adsorption. Meanwhile, the adsorption of Cr by UiO-66@GO was not only adsorbed as monomolecular chemical adsorption, but also surface adsorption. Characterization analysis showed that the adsorption mechanism was related to UiO-66 itself and doped functional materials. Adsorbed metal ions bonded to Zr or carbon formed new complexes. Additionally, the encapsulated method can increase the protection of UiO-55 from surface damage. In all, different hybrid methods cause some differences in the activity and reaction mechanism.

Conflicts of interest

There are no conflicts to declare.

Acknowledgements

This work is supported by the National Key Research and Development Program of China (Grant No. 2019YFC1805904) and Xinjiang Science Fund for Distinguished Young Scholars (2022D01E40).

References

1 K. Zhu, C. Chen, H. Xu, Y. Gao, X. Tan, A. Alsaedi and T. Hayat, Cr(VI) Reduction and Immobilization by Core-Double-Shell Structured Magnetic Polydopamine@ Zeolitic Idazolate Frameworks-8 Microspheres, *ACS Sustainable Chem. Eng.*, 2017, **5**, 6795–6802.

2 H. Li, W. Liu, H. Han and H. Yu, Hydrophilic swellable metal–organic framework encapsulated Pd nanoparticles as an efficient catalyst for Cr(VI) reduction, *J. Mater. Chem. A*, 2016, **10**, 1039.

3 X. Tian, W. Wang, N. Tian, C. Zhou, C. Yang and S. Komarneni, Cr(VI) reduction and immobilization by novel carbonaceous modified magnetic Fe_3O_4/halloysite nanohybrid, *J. Hazard. Mater.*, 2016, **309**, 151–156.

4 H. Cui, Q. Li, Y. Qian, R. Tang, H. An and J. Zhai, Defluoridation of water via electrically controlled anion exchange by polyaniline modified electrode reactor, *Water Res.*, 2011, **45**, 5736–5744.

5 S. Jagtap, M. Yenkie, N. Labhsetwar and S. Rayalu, Fluoride in drinking water and defluoridation of water, *Chem. Rev.*, 2012, **112**, 2454.

6 M. Ali, B. Hamrouni and M. Dhahbi, Electrodialytic Defluoridation of Brackish Water: Effect of Process Parameters and Water Characteristics, *Clean*, 2010, **38**, 623–629.

7 Q. Guo and J. Tian, Removal of fluoride and arsenate from aqueous solution by hydrocalumite via precipitation and anion exchange, *Chem. Eng. J.*, 2013, **231**, 121–131.

8 A. Boubakri, R. Bouchrit, A. Hafiane and A. Bouguecha, Fluoride removal from aqueous solution by direct contact membrane distillation: theoretical and experimental studies, *Environ. Sci. Pollut. Res. Int.*, 2014, **21**, 10493.

9 H. Zhao, B. Zhao, W. Yang and T. Li, Effects of Ca^{2+} and Mg^{2+} on defluoridation in the electrocoagulation process, *Environ. Sci. Technol.*, 2010, **44**, 9112.

10 M. Vithanage, A. Rajapaksha, M. Bootharaju and T. Pradeep, Surface complexation of fluoride at the activated nano-gibbsite water interface, *Colloids Surf., A*, 2014, **462**, 124–130.

11 Y. Tan, W. Zhang, Y. Gao, J. Wu and B. Tang, Facile synthesis and supercapacitive properties of Zr-metal organic frameworks (UiO-66), *RSC Adv.*, 2015, **5**, 17601–17605.

12 P. Cheng and Y. Hu, H_2O-Functionalized Zeolitic Zn (2-methylimidazole)2 Framework (ZIF-8) for H_2 Storage, *J. Phys. Chem. C*, 2014, **118**, 21866–21872.

13 P. Falcaro, R. Ricco, A. Yazdi, I. Imaz, S. Furukawa, D. Maspoch, R. Ameloot, J. Evans and C. Doonan, Application of Metal and Metal Oxide Nanoparticles@MOFs, *Coord. Chem. Rev.*, 2016, **108**, 2726.

14 L. Fang, K. Zhang, X. Li, H. Wu and P. Wu, Preparation of a Carbon-Silica Mesoporous Composite Functionalized with Sulfonic Acid Groups and Its Application to the Production of Biodiesel, *Chin. J. Catal.*, 2006, **33**, 114–122.

15 Z. Ulker, I. Erucar, S. Keskin and C. Erkey, Novel nanostructured composites of silica aerogels with a metal organic framework, *Microporous Mesoporous Mater.*, 2013, **170**, 352–358.

16 Z. Gang, C. Xu, W. Cheng, Z. Qi and N. Wen, Effects of Oxygen Element and Oxygen-Containing Functional Groups on Surface Wettability of Coal Dust with Various Metamorphic Degrees Based on XPS Experiment, *J. Anal. Methods Chem.*, 2015, **25**, 467242.

17 L. Yu, Y. Zhang, B. Zhang, J. Liu, H. Zhang and C. Song, Preparation and characterization of HPEI-GO/PES ultrafiltration membrane with antifouling and antibacterial properties, *J. Membr. Sci.*, 2013, **447**, 452–462.

18 Q. Guan, B. Wang, X. Chai, J. Liu and J. Gu, Comparison of Pd-UiO-66 and Pd-UiO-66-NH_2 catalysts performance for phenol hydrogenation in aqueous medium, *Fuel*, 2017, **205**, 130–141.

19 X. Li, C. Han, W. Zhu, W. Ma, Y. Luo, Y. Zhou, J. Yu and K. Wei, Cr(VI) Removal from Aqueous by Adsorption on Amine-Functionalized Mesoporous Silica Prepared from Silica Fume, *J. Chem.*, 2014, **11**, 1–10.

20 Z. Wang, Y. Xie and C. Liu, Synthesis and Characterization of Noble Metal (Pd, Pt, Au, Ag) Nanostructured Materials Confined in the Channels of Mesoporous SBA-15, *J. Phys. Chem. C*, 2008, **112**, 19818–19824.

21 C. Petit and T. Bandosz, Exploring the coordination chemistry of MOF–graphite oxide composites and their applications as adsorbents, *Dalton Trans.*, 2012, **41**, 4027.

22 L. Li, X. Liu, H. Geng, B. Hu, G. Song and Z. Xu, A MOF/graphite oxide hybrid (MOF: HKUST-1) material for the adsorption of methylene blue from aqueous solution, *J. Mater. Chem. A*, 2013, **1**, 10292–10299.

23 S. Ryu, C. Fonseka, G. Naidu, P. Loganathan, H. Moon, J. Kandasamy and S. Vigneswaran, Recovery of rare earth elements (Lu, Y) by adsorption using functionalized SBA-15 and MIL-101 (Cr), *Chemosphere*, 2021, **97**, 130869.

24 N. Ramsahye, P. Trens and C. Shepherd, The effect of pore shape on hydrocarbon selectivity on UiO-66(Zr), HKUST-1 and MIL-125(Ti) metal organic frameworks: insights from molecular simulations and chromatography, *Microporous Mesoporous Mater.*, 2014, **189**, 222–231.

25 H. Lou, Z. Yuan, Q. Xiang, J. Xu, L. Hui, P. Xu and X. Li, The real-time detection of trace-level Hg^{2+} in water by QCM loaded with thiol-functionalized SBA-15, *Sens. Actuators, B*, 2012, **166–167**, 246–252.

26 C. Petit and T. Bandosz, MOF–Graphite Oxide Composites: Combining the Uniqueness of Graphene Layers and Metal–Organic Frameworks, *Adv. Mater.*, 2009, **21**, 4753–4757.

27 P. Yang, Q. Liu, J. Liu, H. Zhang, Z. Li, R. Li, L. Liu and J. Wang, Interfacial growth of a metal-organic framework (UiO-66) on functionalized graphene oxide (GO) as a suitable seawater adsorbent for extraction of uranium(VI), *J. Mater. Chem. A*, 2017, **5**, 17933–17942.

28 F. Gioia, G. Greco and L. Gibilaro, The effect of a limiting non-key reactant on pseudo first-order reactions in porous catalysts, *Chem. Eng. Sci.*, 1970, **25**, 969–978.

29 X. Wang, J. Pan, W. Guan, J. Dai, X. Zou, Y. Yan, C. Li and W. Hu, Selective Removal of 3-Chlorophenol from Aqueous

Solution Using Surface Molecularly Imprinted Microspheres, *J. Chem. Eng. Data*, 2011, **56**, 2793–2801.

30 Y. Huang, X. Ma, G. Liang, Y. Yan and S. Wang, Adsorption behavior of Cr(VI) on organic-modified rectorite, *Chem. Eng. J.*, 2008, **138**, 187–193.

31 G. Zhang, Z. He and W. Xu, A low-cost and high efficient zirconium-modified-Na-attapulgite adsorbent for fluoride removal from aqueous solutions, *Chem. Eng. J.*, 2012, **183**, 315–324.

32 Y. Wang and T. Liang, Application of lumped-mass vibration absorber on the vibration reduction of a nonlinear beam-spring-mass system with internal resonances, *J. Sound Vib.*, 2015, **350**, 140–170.

33 R. Zhang, J. Zhang, X. Zhang, C. Dou and R. Han, Adsorption of Congo red from aqueous solutions using cationic surfactant modified wheat straw in batch mode: kinetic and equilibrium study, *J. Taiwan Inst. Chem. Eng.*, 2014, **45**, 2578–2583.

34 X. Shi, W. Ruan, J. Hu, M. Fan, R. Cao and X. Wei, Optimizing the Removal of Rhodamine B in Aqueous Solutions by Reduced Graphene Oxide-Supported Nanoscale Zerovalent Iron (nZVI/rGO) Using an Artificial Neural Network-Genetic Algorithm (ANN-GA), *Nanomaterials*, 2017, **7**, 134.

35 S. Subramani, D. Kumaresan and N. Thinakaran, Application of activated carbon derived from waste Delonix regia seed pods for the adsorption of acid dyes: kinetic and equilibrium studies, *Desalin. Water Treat.*, 2016, **57**, 7322–7333.

36 C. Yang, Statistical mechanical aspects of adsorption systems obeying the Temkin isotherm, *J. Phys. Chem.*, 1993, **97**, 7097–7101.

37 J. Fang, Z. Gu, D. Gang, C. Liu, E. Ilton and B. Deng, Cr(VI) removal from aqueous solution by activated carbon coated with quaternized poly(4-vinylpyridine), *Environ. Sci. Technol.*, 2007, **41**, 4748–4753.

38 J. Geng, Y. Yin, Q. Liang, Z. Zhu and H. Luo, Polyethyleneimine cross-linked graphene oxide for removing hazardous hexavalent chromium: adsorption performance and mechanism, *Chem. Eng. J.*, 2019, **361**, 1497–1510.

39 Q. Huang, D. Zeng, S. Tian and C. Xie, Synthesis of defect graphene and its application for room temperature humidity sensing, *Mater. Lett.*, 2012, **83**, 76–79.

40 S. Cai, Y. Zhang, H. Zhang, H. Yan, H. Lv and B. Jiang, Sol-Gel Preparation of Hydrophobic Silica Antireflective Coatings with Low Refractive Index by Base/Acid Two-Step Catalysis, *ACS Appl. Mater. Interfaces*, 2014, **6**, 11470–11475.

41 N. Adhikari, U. Premadasa and K. Cimatu, Sum frequency generation vibrational spectroscopy of methacrylate-based functional monomers at the hydrophilic solid-liquid interface, *Phys. Chem. Chem. Phys.*, 2017, **19**, 21818–21828.

42 I. Kiyoshi, W. Harumichi and N. Yoshiharu, Infrared study of solubilization of carboxylic acid by alkaline earth metal salts of dinonylnaphthalenesulfonic acid in hexane, *J. Colloid Interface Sci.*, 1983, **94**, 229–236.

43 R. Sarmiento-Perez, L. Rodriguez-Albelo, A. Gomez, M. Autie-Perez, D. Lewis and R. Ruiz-Salvador, Surprising role of the BDC organic ligand in the adsorption of CO_2 by MOF-5, *Microporous Mesoporous Mater.*, 2012, **163**, 186–191.